Research in Astron. Astrophys. Vol.0 (20xx) No.0, 000–000 http://www.raa-journal.org http://www.iop.org/journals/raa (LATEX: RAA-2025-0200.tex; printed on November 14, 2025; 1:25)

Mock Observations for the CSST Mission: CPI-C-Instrument Simulation

Gang Zhao 1,2 , Yiming Zhu 1,2 , Jiangpei Dou 1,2 , Yili Chen 1,2 , Zhonghua Lv 1,2 , Bingli Niu 1,2 , Zhaojun Yan 3 , Bo Ma 4,5 and Ran Li 6

- ¹ Nanjing Institute of Astronomical Optics & Technology, Chinese Academy of Sciences, Nanjing 210042, China; gzhao@niaot.ac.cn; jpdou@niaot.ac.cn
- ² CAS Key Laboratory of Astronomical Optics & Technology, Nanjing Institute of Astronomical Optics & Technology, Nanjing 210042, China
- ³ Shanghai Astronomical Observatory, Chinese Academy of Sciences, Shanghai 200030, China
- ⁴ School of Physics and Astronomy, Sun Yat-sen University, Zhuhai, Guangdong 519082, PR China
- ⁵ Center of CSST in the great bay area, Sun Yat-sen University, Zhuhai, Guangdong 519082, PR China
- ⁶ School of Physics and Astronomy, Beijing Normal University, Beijing 100875, China Received 20xx month day; accepted 20xx month day

Abstract To support the development of the data processing pipeline and the scientific performance assessment for the Cool Planet Imaging Coronagraph (CPI-C) on the Chinese Space Station Survey Telescope (CSST), we have developed the end-to-end instrument simulation program, CPISM. This paper details the core modules of CPISM that simulate the CPI-C instrument, focusing on the simulation of the high-contrast imaging optical system and the visible-band science camera. We modeled key optical components, such as the transmission apodizing filter, the wavefront corrector, and the focal plane mask using the HCIPy package. A 10^{-8} contrast dark hole region, consistent with design specifications, was simulated using the Electric Field Conjugation (EFC) optimization method, and broadband observation effects were considered. For the science camera, which is an electron multiplying charge-coupled device (EMCCD), we established a detailed model encompassing photon collection, charge transfer, electron multiplication (EM), and readout processes, based on test data. This model simulates complex instrumental features including dark current, charge transfer efficiency, clock-induced charge, multiplication noise factor, and various readout effects like striping and drift. We also proposed and validated an improved statistical model for the EM process to enhance simulation efficiency. CPISM can generate simulated images containing rich instrumental details, closely similar to the expected real observational data, thus laying the foundation for the development and verification of CPI-C data processing algorithms and preparations for future scientific research.

Key words: planets and satellites: detection — instrumentation: high angular resolution — methods: numerical

1 INTRODUCTION

The Cool Planets Imaging Coronagraph (CPI-C¹, Dou et al. 2025) is one of the five backend instruments of the Chinese Space Station Survey Telescope (CSST, CSST Collaboration et al. 2025). It is designed for ultra-high contrast detection and multi-band photometry studies of extrasolar planets and circumstellar disks in visible to near-infrared wavelengths. Utilizing pupil apodization (Ren & Zhu 2007; Ren et al. 2010), and phase modulation methods (Dou & Ren 2016), CPI-C creates two dark regions with a contrast ratio up to 10^{-8} near the center of the star's image. In these dark regions, multi-band images of extrasolar planets can be obtained. Subsequently, spectral fitting can be used to infer their atmospheric spectra and physical properties. The construction of the coronagraph instrument is currently underway, and the development of the data reduction pipeline and preliminary scientific research are also in progress. To support these tasks, we have developed an end-to-end CPI-C image simulation tool - CPISM (CPI-C Image Simulator). ². The CPISM is developed using the Python language. When users input target information such as stellar spectral type and planetary radius, as well as instrumental parameters like exposure time and observation bands through the command line, CPISM can generate simulation images that match the format of real data for subsequent processing and analysis.

In modern space astronomy projects, simulation plays an increasingly important role. Simulation tools, integrated with instrument test results, provide a research foundation for target selection, observation planning, and the preparation of observation data processing procedures. The James Webb Space Telescope (JWST) serves as an excellent example. Years before its launch, high-contrast simulation programs, as well as camera simulation programs, point spread function (PSF) simulation programs, and the instrument effect simulation tools were prepared (Girard et al. 2018). The JWST pipeline has also been developed based on simulation data (Gordon et al. 2022). The thorough preparation has led to a rapid scientific output. For instance, the direct imaging observation of the exoplanet VHS 1256 b (Miles et al. 2023) proceeded smoothly and rapidly following the observation on July 4, 2022. The complete workflow, including initial data reduction, high-contrast data processing, target photometry, spectral fitting, and determination of planetary physical properties, was accomplished in just two months, with the related paper submitted by September 3, 2022. Similarly, for the CGI instrument of the Roman Space Telescope (under construction), a series of simulation tools were developed (Douglas et al. 2020), including planetary target transmittance spectrum models, coronagraph high-contrast simulation, and complete end-to-end simulation. These simulation tools have been used to validate data processing algorithms (Ygouf et al. 2021) and determine exoplanet parameters (Turnbull et al. 2021).

As an end-to-end simulation tool, CPISM consists of an observation target simulation module, an observation effect simulation module, a high-contrast imaging simulation module, and a camera simulation module. The core objective of the CPISM is to provide test images for the CPIC data reduction pipeline. The pipeline primarily focuses on instrumental effects correction. It takes the level 0 data (raw data) from CPI-C as input, and processes this data to correct detector effects and remove background light and cosmic ray influences, generating level 1 image data. To meet the needs of processing detector effects, CPISM thoroughly models the EMCCD camera, considering the results of camera qualification tests. The simulation covers various stages of the camera's operation, including photon collection, vertical transfer, EM amplification, and readout. To address the needs of cosmic ray processing, the CPISM constructs a cosmic ray model suitable for the CPI-C's camera, based on the characteristics of cosmic rays from Hubble Space Telescope observations (Heyer et al. 2004; Miles et al. 2021). Currently, configuration testing of the CPI-C data reduction pipeline is being carried out based on data generated by

¹ In Table C.1, we list all the acronyms in the paper.

 $^{^2~{\}rm https://csst\text{-}tb.bao.ac.cn/code/csst\text{-}sims/csst_cpic_sim}$

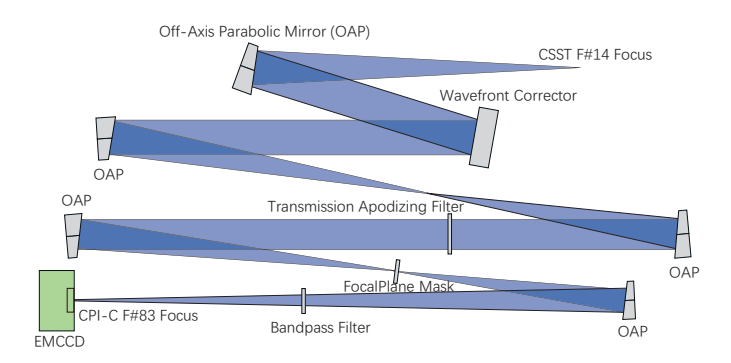


Fig. 1: The schematic of the CPI-C optical layout.

CPISM. Furthermore, CPISM is also designed to validate CPI-C science (e.g. Bao et al. 2025). To this end, the CPISM semi-quantitatively simulates high-contrast imaging dark holes with a contrast ratio of 1×10^{-8} , as well as the reflected spectra of exoplanets with different metallicities and cloud characteristics.

The CPISM will be introduced in two papers. In the first paper of the series, Zhu et al. (2025) provided an overall introduction to the CPISM, as well as the details of simulation of observation targets and the use of simulated data for scientific research. In this paper, we introduce the simulation of the CPI-C instrument, focusing on the high-contrast imaging module and the visible band camera. The article is organized as follows: In Section 2, we present the numerical models of the core components of the high-contrast imaging simulation module, including the apodized pupil filter, high-order wavefront corrector, and focal plane mask. We explore methods to optimize the high-contrast dark zone, and achieve a PSF similar to the instrument measurement results. In Section 3, we introduce the model of the EMCCD serving as the visible band scientific camera of CPI-C, and provide a detailed introduction to the modeling of the core process of electron multiplication. In Section 4, we summarize the paper.

2 SIMULATION OF OPTICS OF HIGH CONTRAST IMAGING

CPI-C achieves high-contrast imaging of 10^{-8} through its core components: the wavefront corrector (which is a deformable mirror), and the focal plane mask. The schematic of its optical layout is shown in Figure 1.³ The wavefront corrector and the apodizing filter are located at the conjugate position of the pupil plane in the optical path, modulating the amplitude and phase of the wavefront; the focal plane mask is at the secondary focal plane of the optical system, blocking the starlight and the cross-shaped diffraction structures. After passing through the secondary focal plane, the light is focused by an off-axis parabolic mirror and finally imaged on the visible light imaging camera at the F#83 focus.

We use the Python-based HCIPy package (Por et al. 2018) to model and simulate high-contrast devices and the optical propagation. During the modeling process, various device parameters, such as the spot size at the DM and the number of DM actuators, are based on design values. However, details such as the aberrations in the system and the DM surface shape when creating the dark zone are not based on actual measurements from the actual optics, which means that the simulated PSF does not completely match the PSF of the real instrument but has similar shapes, and parameters, such as contrast and inner working angle.

³ This schematic is a simplification of the actual optical path; the real optical path also includes tip-tilt correction mirrors, reflectors, beam splitters, as well as wavefront sensing branch and near-infrared imaging branch, which are not depicted in the schematic.

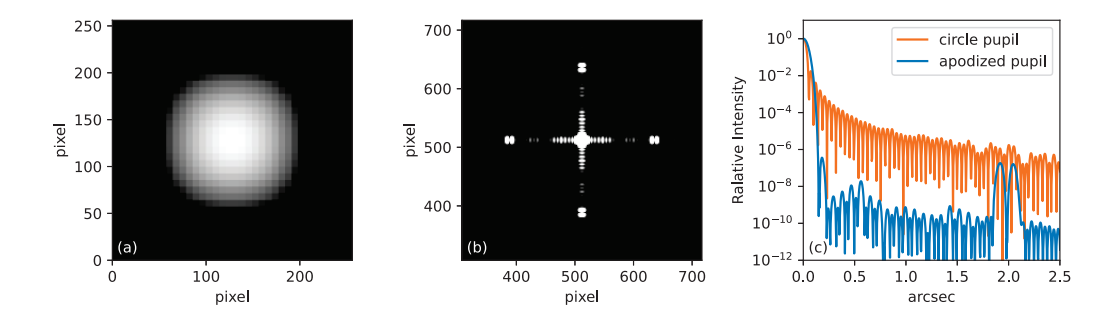


Fig. 2: Model and simulation results of the Apodizing Filter. a) Transmittance distribution of the Apodizing Filter, with white representing higher transmittance. b) The theoretical point spread function after pupil apodization at 662nm. Photon noise and Readout noise are not considered in the image c) The contrast curves after apodization (blue line) compared to that of an apodized circular aperture. The contrast curve is along the square diagonal direction.

2.1 Modeling the Core Components of High Contrast Imaging

2.1.1 The Transmission Apodizing Filter

When the light of a point source passes through the telescope, the bright diffracted light can drown out the faint planetary light, making it difficult to directly image the planet. The transmission apodizing filter located at the conjugate pupil plane of the telescope, by modulating the electric field intensity on the telescope's pupil, can alter the energy distribution of the PSF, and suppress the diffraction from the telescope aperture. The transmission apodizing filter is designed based on the principle of Ren & Zhu (2007), and is composed of 32 strips with different transmittance in both the horizontal and vertical directions. As shown in Figure 2a, the central strip has a higher transmittance, with lower transmittance on the sides. In the CPISM, we construct it using the Field class from the HCIPy module, and the transmittance of the apodizing filter can be configured through the apm.fits file in the refdata directory. The filter model used in simulation is based on the design values and includes random biases to reflect the influences of manufacturing errors. Figures 2b and 2c show the theoretical apodized PSF image at 662 nm and the contrast curve, respectively. It can be seen that the filter, while increasing the size of the central bright spot and the cross structure, can effectively suppress diffracted light, achieving a contrast below 10^{-8} . Additionally, multiple orders of diffraction spots can be observed in the image, which can be used for subsequent calibration of target brightness and is an advantage of a step transmission filter.

2.1.2 The Wavefront Corrector

In CPI-C's optical path, a 952-actuator Micro-electromechanical Systems (MEMS) deformable mirror (DM) is used as a wavefront corrector. It has two purposes. Firstly, it is used to correct residual aberrations in the system, which may be introduced by the optical path of the telescope or caused by temperature changes and other quasi-static low-order aberrations within the system. Secondly, the wavefront corrector can form a specific surface shape to create a high-contrast imaging dark zone at the focal plane, for details, see Dou & Ren (2016). We model the DM using the *DeformableMirror* module in the HCIPy package. Since this is a semi-quantitative simulation, we have not measured the actual DM response function but used the built-in DM response function provided by the HCIPy package.

In our simulations, we did not model in detail the optical system of the telescope, such as the imaging quality and tracking accuracy, because the CPI-C integrates wavefront correction and tracking subsystems. These subsystems are designed to compensate for telescope aberrations and tracking errors. During the closed-loop correction process for high-order wavefront aberrations, control accuracy is mainly limited by the precision of aberration detection and control. In the semi-quantitative simulation, which did not model the closed-loop correction process, we introduce a random offset to the DM control voltage to represent control errors. The magnitude of the random offset can be set via parameters.

2.2 High Contrast Optimization

The aberrations can significantly degrade image quality as well as the contrast in the CPI-C system. Aberrations are induced by various sources, including the manufacturing process of optical components, thermal changes and gravitational effects. Under the influence of aberrations, the PSF corresponding to the apodizing filter is estimated to only achieve a contrast of 10^{-6} . For the CPI-C instrument, a high contrast calibration mode has been designed. In this mode, Stochastic Parallel Gradient Descent (SPGD) algorithm (Dou & Ren 2016; Dong et al. 2011) is employed to correct the aberrations, and optimize high-contrast imaging dark zones of 10^{-8} at the focal plane. The dark zones are square-shaped, located on one side of the Point Spread Function (PSF) core. Each square region spans the angular separation range from 3 to $16 \ \lambda/D$ under theoretical optimal performance. For observations at 662 nm, this corresponds to a physical range of approximately 0.27" to 1.0" from the central star.

In our semi-quantitative simulation, to obtain the optimized shape of the Wavefront Corrector, we did not use the SPGD algorithm adopted by the instrument but used a more efficient Electric Field Conjugation (EFC) method (Matthews 2017) for optimization, to form dark holes similar to the design value. The exploration of the EFC method in pupil apodization high-contrast imaging systems may provide a reference for the design of next generation of CPI-C instrument.

Before optimization, it is necessary to model the system's aberrations. We conducted a qualitative simulation of the aberrations, which have phase and amplitude components when they propagate to the pupil plane. Under the influence of these aberrations, speckles appear around the PSF (see the example PSF of 662nm in Figure 3a). The resulting contrast, indicated by the blue solid line in Figure 3c, is about 10^{-6} . This value is on the same order of magnitude as the instrument design specification.

The details of the process of EFC can be found in the Appendix A. After EFC correction, the final optimized imaging dark zone is shown in Figure 3b at 662nm, and the contrast curve is shown by the red solid line in Figure 3c. It can be seen that the final contrast of the dark zone is 10^{-8} , consistent with the instrument's design. Compared to the contrast curve of the PSF without wavefront aberrations (orange solid line in Figure 3c), the optimization process successfully corrected the speckles in the dark holes, achieving contrast levels similar to the aberration-free PSF.

The DM primarily influences the inner part of the PSF (< 1.2'', low spatial frequency region), while leaving the outer part (high spatial frequency region) largely unchanged. This limitation is due to the Nyquist sampling theorem; for a DM with 32 actuators across the pupil diameter, it can effectively control aberrations only within a radius of approximately $16\lambda/D$ in the image plane, thus defining the system's high-contrast outer working angle. During the dark zone optimization process, by defining specific optimization regions, we can generate dark zones located on the same side of the PSF, such as the right side or the top. When running CPISM, dark zones in different orientations can be selected by setting the <code>dm_volt_index</code> parameter in the configuration file. However, it is not able to achieve centrosymmetric dark zones. This limitation is primarily because the CPIC system has only a single DM, which cannot provide simultaneous correction of both amplitude and phase aberrations in the system. To form centrosymmetric dark zones, at least two DMs are required (Pueyo et al. 2009). For

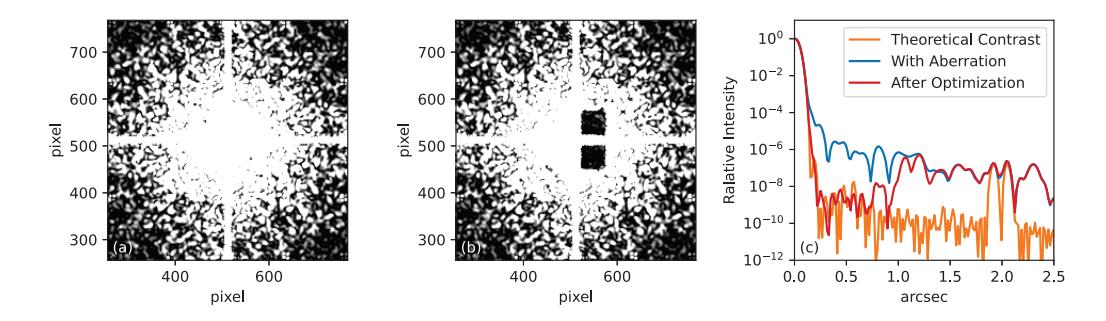


Fig. 3: (a) The PSF with aberrations at the first focal plane of CPI-C at 662nm. Photon noise and readout noise are not considered. (b) 10^{-8} dark zone after high contrast optimization at 662nm. (c) The contrast curves. Orange line indicates the theoretical curve of the system. Blue line indicates the case with aberrations, and Red line the contrast curve after optimization. The contrast curve is along the square diagonal direction.

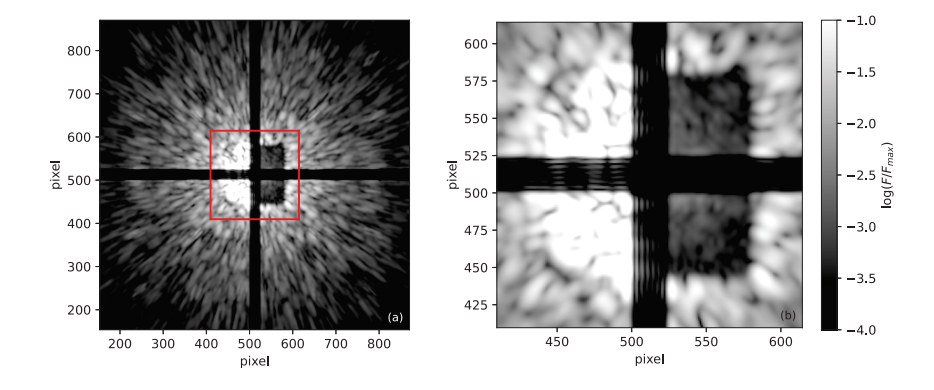


Fig. 4: Final focal plane image of the CPI-C system for a G0V star at the F662 band . Panel (a) displays the entire focal plane, while Panel (b) presents a detailed zoom-in view of the central region, as indicated by the red square in Panel (a). Note that the dark hole is based on simulations, and it will be calibrated to align with the future ground and on-orbit test results.

instance, the CGI instrument on the Roman Space Telescope utilizes two DMs, enabling the formation of centrosymmetric annular or fan-shaped dark zones (Trauger et al. 2016).

In addition, there are undulating speckle noise within the dark zone, which is also consistent with the measurement. Subsequent high-contrast algorithms such as Angular Differential Imaging (ADI, Marois et al. 2006), Locally Optimized Combination of Images (LOCI, Lafreniere et al. 2007), or Optimized Image Rotation and Subtraction (OIRS, Dou et al. 2015) can be used to suppress the speckles. The simulated images generated by CPISM can also provide test data for developing these speckle-reduction algorithms for CPI-C.

2.3 Focal Plane Mask

From Figure 3, it can be seen that there is a cross-shaped diffraction structure in addition to the star. This structure is caused by the vertically stacked bands in the transmission modulation filter. During visible light imaging, both the star and this diffraction structure can easily saturate and cause overflow. To prevent overflow, a custom focal plane mask is equipped to shield the light of the star and its cross-shaped diffraction pattern. The focal plane mask was

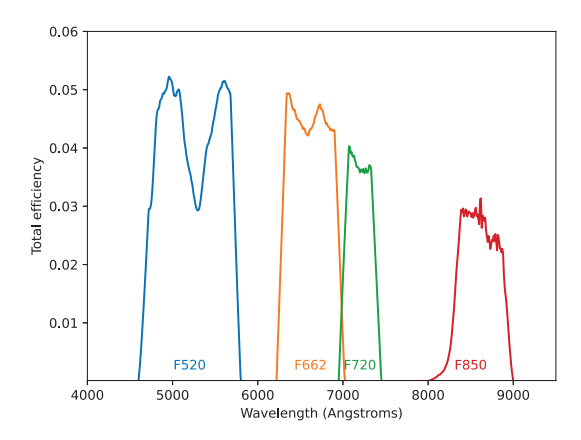


Fig. 5: The total efficiency curve of the four visible light bands of CPI-C.

fabricated by coating chromium metal film on a fused silica substrate, creating opaque cross arms with a width corresponding to 0.4 arcsecond, thereby shielding light within a half-width of $3\lambda/D$ (approximately 0.2 arcseconds) at the F662 band. The throughput in the masked region measures approximately 10^{-6} . Since the focal plane scale is 1.615×10^{-2} "/pix, the masked cross-shaped region spans ~ 24 pix in the final image.

Our simulation of the focal plane mask and its diffraction effects follows the principle of Dou & Ren (2016). Using HCIPy's ComplexSurfaceApodizer module, we modeled the mask. For the light through the mask, the wavefront amplitude will be reduced by 10^{-6} in the blocked areas. We then calculated the pupil plane wavefront using HCIPy's FraunhoferPropagator. At this pupil plane, high-frequency components induced from the mask were blocked, to simulate the finite aperture of the imaging lens. Light then propagated to the secondary focal plane where science cameras capture images. Figure 4 shows the result. It can be observed that the star and the cross-shaped diffraction are effectively blocked, leaving only the mask's own diffraction pattern in the obscured regions.

2.4 Observation Band

CPI-C is utilized to conduct observations across four visible light bands (F520, F662, F720, and F850). Figure 5 displays the overall efficiency curve of each band, considering the designed transmission curve of the filters, the measured throughput of the other optical elements in the system and the theoretical quantum efficiency of the camera. The selection of the four-band system is described in detail in a companion study (Zhu et al 2025, submitted). Given the wavelength range of approximately 100 nm for each band, it is necessary to account for the effects of broadband filtering in our simulation program. To this end, each observation band is divided into M narrower sub-bands, where M is an adjustable parameter. For each narrow subband, we generate monochromatic images based on the central wavelength position λ_i , where i ranges from 1 to M.

Let $I(\lambda_i)$ represent the monochromatic image observed at the wavelength λ_i . For each narrow band, we calculate the spectral energy distribution (SED) within the band based on the target's spectral curve $S(\lambda)$ and the instrument's efficiency curve $T(\lambda)$. Mathematically, for each narrow band, the SED can be expressed as:

$$SED_i = \int_{\lambda_{i-1/2}}^{\lambda_{i+1/2}} S(\lambda)T(\lambda) d\lambda$$
 (1)

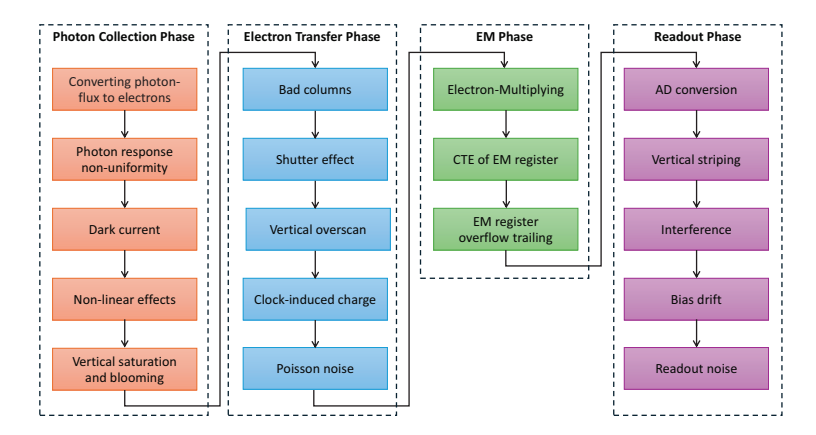


Fig. 6: The flowchart of the EMCCD simulation process.

where $\lambda_{i-1/2}$ and $\lambda_{i+1/2}$ denote the lower and upper wavelength boundaries of the *i*-th narrow band, respectively.

Thereafter, we employ the calculated SED values to weight and superpose the corresponding monochromatic images, thereby generating a broadband image. The weighting and superposition process is represented as:

$$I_{\text{broad}} = \sum_{i=1}^{M} w_i \cdot I(\lambda_i) \tag{2}$$

Here, w_i is the weight of the *i*-th band, determined by the SED value of that band:

$$w_i = \frac{SED_i}{\sum_{j=1}^{M} SED_j} \tag{3}$$

By employing this method, we are able to generate images that take into account the effects of broadband filtering. In Figure 4, the image of a G0V star at F662 band is shown. It can be observed that the speckle pattern is elongated into a linear shape. In subsequent analysis, we may be able to utilize such speckle structures to analyze the spectrum of the star.

3 SIMULATION OF THE VISIBLE BAND CAMERA

The CPI-C module uses an EMCCD (Electron Multiplying Charge-Coupled Device) as the imaging detector for the visible focal plane. EMCCDs are widely applied in the observation of faint targets and space astronomy (Tulloch & Dhillon 2011), such as the CGI module of the Roman Space Telescope (Daigle et al. 2022). The EMCCD employs electron multiplication technology, which effectively enhances detection efficiency and reduces the equivalent read noise. Before being read out, electrons pass through a series of electron multiplication registers (the number is 604 for the EMCCD used in CPI-C), which contain high-voltage potential wells. When electrons fall into these wells, they have a certain probability of causing an avalanche effect, thereby amplifying the collected signal. In an ideal scenario, if the electron multiplication gain is denoted as g_A , the equivalent read noise can be reduced to the level of $1/g_A$.

In the CPI-C simulation program, the EMCCD is modeled, including the photon collection phase, electron transfer phase, multiplication phase, and readout phase. At each stage, various instrumental effects are taken into account to ensure that the final simulated image closely resembles the real image. The flowchart of the entire simulation process is shown in Figure 6.

3.1 Photon Collection Phase Modeling

The collection phase refers to the process where the camera receives photons, converts them into electrons, and accumulates them in the potential wells of the collection area. In the CPI-C simulation program, the photon collection model procedure is as follows:

- 1. First, based on the instrument's throughput curve and the chip's quantum efficiency curve, the 1024×1024 focal plane image, generated by the high-contrast imaging module with units of photons, is converted into an image with units of electrons.
- 2. Utilizing flat-field reference data from the configuration file, the spatial non-uniformity of the photoelectric response across the chip's pixels is accounted for.
- 3. According to dark-field reference data from the configuration file, dark current and hot pixels are added to the image. The camera has 16 dark reference columns on each side of the image area, 6 rows of dark reference region on the top of the image area, as well as 2 rows on the bottom. The dark reference area and transition region have the same structure as the imaging area, but with an aluminum coating that shields the light. As its name suggests, the dark reference region can be used to estimate the level of dark current of the chip. The image region and dark regions have the total size of 1056×1032 .
- 4. A non-linear response to light intensity is added. Currently, in the simulation program, we apply a uniform non-linearity coefficient to the entire image, not considering variations between different pixels.
- 5. When the number of collected electrons exceeds the full well capacity, the overflowing charge will spill vertically.

3.2 Image Transfer Process Modeling

The EMCCD chip used in the CPI-C requires three vertical transfer operations to capture an image. The first step involves an initial overall transfer at the start of exposure to clear the electrons from the collection area. The second step occurs when the set exposure time has elapsed; the upper half of the chip's collection area transfers the accumulated electrons vertically to the lower half's storage area, which is structurally similar but with an aluminum coating that shields the light. The third step is the line-by-line transfer and readout. These steps enable precise control over the exposure time of each pixel, achieving what is known as an electronic shutter. The simulation of the transfer phase includes the following effects:

- 1. **Bad Column Effect**: When there are defective pixels in the collection or transfer area that affect the transfer process, this impacts all or part of the pixels in that column, manifesting as a vertical column of abnormal points in the image. In the simulation, the position of bad pixels can be configured to simulate bad columns.
- 2. Shutter Effect: As the image transfers from the collection area to the storage area, photoelectric conversion in the collection area continues, leaving a vertical trail in the image. This effect, also known as the smear effect, is related to the transfer speed and is particularly noticeable under strong light and short exposure. The transfer frequency is 500 kHz, effectively providing a 2 ms (1088 row / 500 kHz) short exposure for each position in that column.
- 3. Overscan: After the entire image has been fully transferred during the readout process, an overscan operation is performed, involving an additional 18 transfers.
- 4. Clock Induced Charge (CIC) Effect: The CIC effect is a particularly important source of noise in EMCCDs. During the readout transfer process of a CCD, there is an extremely small probability that an extra electron will be generated in the potential well, also called a CIC event. For traditional CCDs, this effect is much smaller than the read noise and is generally not considered separately. However, for EMCCDs, the CIC charge will be amplified by subsequent multiplication registers, becoming a significant factor affecting the equivalent

read noise of EMCCDs, making it particularly important in our EMCCD modeling. In the CPI-C simulation program, CIC charge is about $0.2e^-/\mathrm{pixel/frame}$, and the pattern can be configured by a reference image.

5. **Poisson Randomness**: The electrons from the photoelectric collection process as well as dark current and CIC all follow Poisson distributions. Due to the additive property of the Poisson distribution, Poisson(x + y) = Poisson(x) + Poisson(y), during the transfer phase, we uniformly add Poisson noise to all electrons.

3.3 Electron Multiplication Stage Modeling

3.3.1 EM register modeling

The CPI-C simulation program includes a section of simulation code for the EM multiplication process based on the gain register model. This code, which is an adaptation of the IDL code from Tulloch (2010) into a Python version, accounts for both EM multiplication effects and charge transfer inefficiency (CTI) effects. The specific process is as follows:

- 1. For the total EM gain g_A , the multiplication coefficient for each gain register is calculated as $g_i = \exp(\ln(g_A)/N)$, where N = 604 is the count of EM registers .
- 2. The electron multiplication process is considered as a Bernoulli process, where each electron has the same probability $p = g_i 1$ of generating additional electrons, and the probability for each electron is independent. For m electrons, the number of electrons after multiplication by an EM register follows the Binomial distribution 1 + B(m, p).
- 3. Let the charge transfer inefficiency (CTI) be q. After each transfer, the remaining electrons in the register also follow a binomial distribution B(m,q).
- 4. By modeling the 604 registers, one can obtain the number of electrons within a pixel after multiplication. Modeling all 1024×1024 pixels of the chip allows one to obtain the complete image after multiplication.

3.3.2 Statistic Model of Electron Multiplication

Simulation based on the gain register model is very time-consuming. For instance, simulating a set of one hundred bias frames takes more than 24 hours. To improve the efficiency of the simulation, the CPISM also includes a set of simulation methods based on the statistical distribution of the complete multiplication process. The probability distribution of the output n, for an input of m (integer) electrons in an EMCCD has been studied. In Basden et al. (2003), this distribution is considered approximately as a Gamma distribution, and Tubbs (2003) provided a more general form of this distribution as:

$$P(n; m, g_A) = \frac{(n-m+1)^{m-1}}{(m-1)!(g_A - 1 + 1/m)^m} \exp\left(-\frac{n-m+1}{g_A - 1 + 1/m}\right),\tag{4}$$

By comparing with the simulation results of the complete gain register model, it is found that these two distributions fit well under high gain conditions, but have a significant difference under low gain conditions. To correct the difference at low gains, we introduced a correction factor c to the Gamma distribution, and express the form of this distribution as:

$$P(n; m, g_A) = \frac{(n - m_0)^{m-1}}{(m-1)!(cg_A)^m} \exp\left(-\frac{n - m_0}{cg_A}\right),\tag{5}$$

where c is the correction factor

$$c = \left[\left(1 - g_A^{-1} \right) \left(2g_A^{-1/N} - 1 \right) \right]^{1/2}, \tag{6}$$

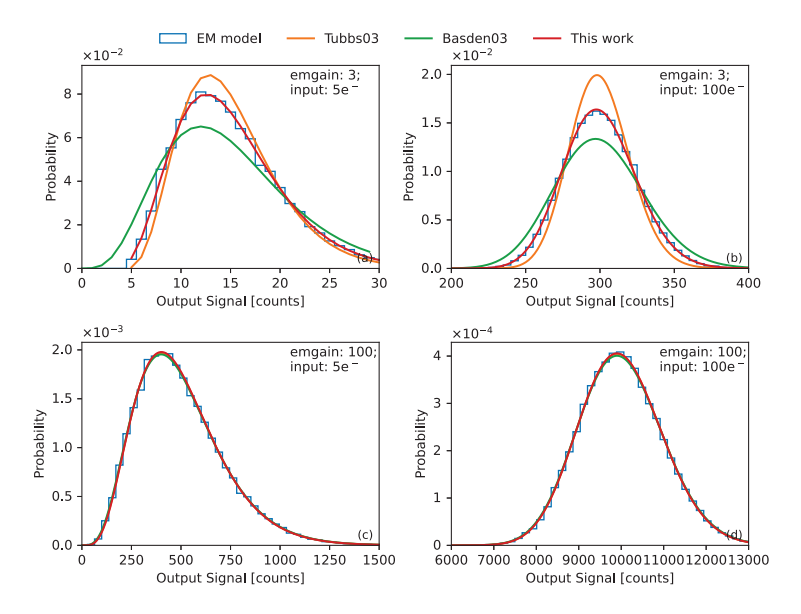


Fig. 7: Distribution of the output signal of electron multiplication in the EMCCD. The red line represents the theoretical distribution as described by Equation 5. The orange and green lines correspond to the distributions reported by Tubbs (2003) and Basden (2003), respectively. The blue step-type histogram illustrates the statistical results from the Monte Carlo simulation of the electron multiplication registers.

 $m_0 = (1 - c)g_A m$, and N is the number of EM registers.

In Figure 7, we plot the distribution of output electrons for an input of m = 100 and m = 5 electrons at different EM gains. It can be observed that the output distribution is close to a normal distribution curve, and the center of the distribution is located approximately at $g_A \cdot m^4$. For higher gain $(g_A=100)$ situations, all three theoretical distributions are similar to the distribution provided by the complete register simulation. However, for low gain cases such as $g_A = 3$, our formula (Equation 5) can better reflect the noise distribution after multiplication.

For EMCCD detectors, the concept of noise factor F is introduced, which represents the relationship between the standard deviation of the input signal $\sigma_{\rm in}$, and that of the output signal $\sigma_{\rm out}$.

$$F = \frac{\sigma_{\text{out}}}{\sigma_{\text{in}} g_A} \tag{7}$$

According to Robbins & Hadwen (2003), the noise factor takes the following form:

$$F^{2} = \frac{1}{q_{A}} + 2(g_{A} - 1)g_{A}^{-\left(\frac{N+1}{N}\right)}$$
(8)

It can be seen that when the EM gain is large, F is approximately equal to $\sqrt{2}$, and when $g_A = 1$, F = 1. Our simulation program can provide an accurate simulation of noise characteristics, which is crucial for the development of camera calibration procedures. In this calibration, the determination of parameters F, as well as the photon transfer curve (PTC), system gain, and EM gain all depend on the noise distribution. Therefore, ensuring the accuracy of simulation results is of great importance for the verification of subsequent camera calibration procedures.

⁴ For the distribution of Equation 7, the mean value is $g_A m$, while the mode (the peak position where the probability reaches maximum) is $g_A(m-c)$, indicating a left shift of the distribution center relative to the mean

3.3.3 EM gain - voltage relationship

The multiplication in an EMCCD is controlled by the voltage applied to the multiplication register. According to Robbins (2009), the relationship between EM gain g_A and voltage V_{EM} satisfies the following equation:

$$g_A = \exp\left[N\beta \exp(\gamma V_{EM})\right],\tag{9}$$

where γ is a parameter of the chip itself, related to the design of the multiplication register and the number of registers, β is related to temperature and aging effect of the chip. It can be seen that the degree of EM gain is very sensitive to the voltage, with the increase rate surpassing exponential relationships. For the camera hardware, a control parameter (hereafter E_{in}) from 1 to 1024 is injected to change the multiplication voltage. Calibrating this relationship is essential in the data reduction pipeline, thus modeling this relationship is necessary for the simulation program.

The model is built based on the actual testing results of the visible band camera of the CPI-C qualification unit. As the first step in the test, we use an oscilloscope to measure the relationship between E_{in} and the multiplication voltage V_{EM} . We found that the two variables exhibit a linear relationship. Using the polyfit function from the NumPy package with the parameter deg=1, we fitted the relationship between $V_{\rm EM}$ and $E_{\rm in}$ as: $V_{EM} = -1.828 \times 10^{-2} \, \rm V \times 10^{-2}$ $E_{in} + 43.61 \,\mathrm{V}$. The second step is to cool the camera to different temperatures and calibrate the EM gain g_A versus V_{EM} by imaging a point source of the same intensity. We employed the curve_fit function from the SciPy library to perform data fitting based on Equation 9, and obtained the values of β and γ . The fitting result shows that $\gamma=0.2465$ for all temperatures (T), and $\beta=-4.790\times 10^{-9}\,\frac{T}{1^{\circ}C}+1.330\times 10^{-7}$. In this way, a model of the relationship between electron multiplication and voltage at different temperatures is obtained. Panel (a) of Figure 8a shows the relationship between voltage and multiplication gain at different temperatures. The blue, orange, and green lines represent the EM gain model at temperatures of -40°C, -60°C, and -80 °C, respectively. The dots indicate the measured results of the CPI-C visible band camera. It can be seen that the model and measurement fit each other well. As the temperature decreases, the same voltage corresponds to a higher EM gain, and the trend is consistent with the feature of EMCCD.⁵

~-79.25°C In the testing, we also found that during continuous rapid high EM gain exposure, the temperature of the chip would rise, and the actual EM gain would decrease under the same E_{in} . This phenomenon may need to be calibrated and corrected in the pipeline, thus we have added a simple temperature model of the camera to the simulation program. When imaging, the camera temperature will rise slightly, with the rate of temperature increase related to the EM voltage and readout frame rate. After exposure is stopped, the camera temperature decreases according to Newton's law of cooling. Figure 8b shows an example of the camera temperature change curve under the influence of this temperature model. The red curve shows the camera temperature evolution during sequential exposures at $E_M = 200$ (EM gain ~ 563). The initial temperature of the camera is -80°C. The sequence begins with 100 frames of 1ms exposures (total duration \sim 40s since the readout overhead is 0.365s), causing a temperature rise of \sim 1.7°C. After a 30-second pause where the temperature drops to \sim -79.25°C. Then the camera takes 100 frames of 1s exposures. During this slower exposure phase, the temperature increases by only ~ 0.25 °C. The blue curve displays the identical exposure sequence at $E_M = 400$ (EM gain \sim 13), which has similar trends but lower peak temperatures due to less heating from the lower EM voltage.

It should be noted that the model related to this effect is a qualitative model and has not been calibrated with actual measurements. The main purpose is to assess the impact of such effects on calibration data processing. If this effect does not need to be added in the simulation, it can be turned off by changing the relevant parameters in the configuration file.

5

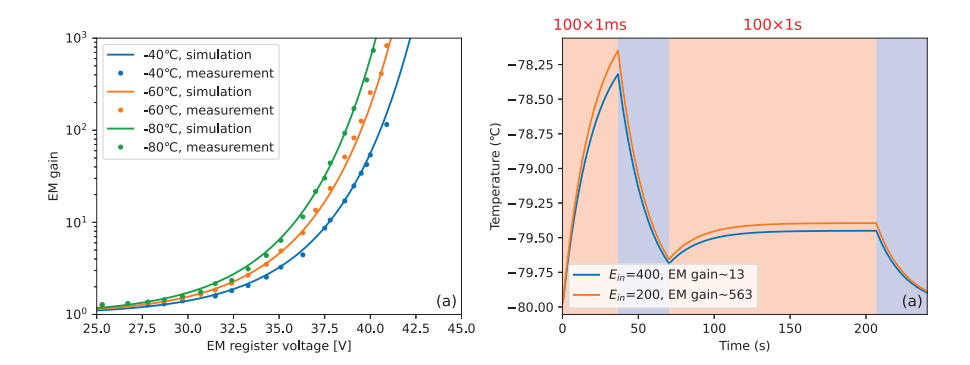


Fig. 8: (a) Relationship between EM gain and multiplication voltage. The blue, orange, and green lines represent the EM gain model at temperatures of $-40\,^{\circ}$ C, $-60\,^{\circ}$ C, and $-80\,^{\circ}$ C, respectively. The dots indicate the measured results of CPI-C's visual band camera. (b) Example of the camera temperature change curve during sequential exposures consists of 100 frames of 1ms exposures and 100 frames of 1s exposures. The red and blue lines represent the cases with $E_M = 200$ (EM voltaEM gain of approximately 563) and $E_M = 400$ (EM gain of approximately 13), respectively.

3.4 Readout Process Modeling

When a light signal passes through the EMCCD imaging chip, it is converted into an electrical signal, which is then amplified by the front end, converted by an AD converter, and read out as a digital signal. The coronagraph visible light imaging camera uses the LM98640 chip for analog-to-digital conversion (ADC). EMCCD readout modeling includes several parts such as ADC, vertical striping, interference signals, background and background drift, and readout noise.

It should be noted that the camera's interference is added based on the images tested when the visible light camera was not integrated, and there will be differences in the integrated state, which can be adjusted after the final qualification unit test of CPI-C.

- 1. Prescan and Overscan. Sixteen non-imaging columns (8 on each side) are read from the left and right edges of the sensor, outside the physical imaging area. These regions are vertical prescan and overscan columns, and can be used for readout noise and bias offset correction. The final image dimensions are 1088 (width) \times 1050 (height) pixels, including these reference columns.
- 2. AD Conversion. According to actual measurements, the coronagraph ADC module converts 59 electrons after electron multiplication into one ADU, i.e., the system conversion gain G_s at $g_A = 1$ is $59e^-/$ ADU.
- 3. Vertical Striping. The LM98640 chip has two readout taps that alternately perform readout. Due to slight differences between the two taps, vertical stripes will form on the image.
- 4. Interference. During the camera's readout process, random horizontal stripes appear in the image due to interference from the ground line. We measure the power spectrum of these random horizontal stripes from test images and generate simulated stripes based on the power spectrum and a random phase.
- 5. Based on the test results, we observed that the bias level of the camera drifts during imaging. Specifically, a random drift with $\sigma \approx 3$ ADU is observed. Additionally, the bias level decreases when using high EM gain. Both of these effects are modeled in CPISM.
- 6. Finally, in the simulation, we add Gaussian-distributed readout noise to the image.

3.5 Example Images

In Figure 9, we present examples of four simulated images. Subfigure (a) shows a zero-exposure bias frame with a multiplication gain of 10, primarily reflecting the readout characteristics of the camera. Horizontal and vertical stripes can be clearly seen. Subfigure (b) displays a bias frame with an EM gain of 500, where the clock-induced charge (CIC) is amplified by the EM gain, resulting in scattered bright spots across the image. In Subfigure (c), we illustrate a 10-second exposure image of a 0th-magnitude star observed by the system. The diffraction pattern of the star and the 10^{-8} high-contrast dark holes are clearly observed. Subfigure (d) demonstrates the imaging of a 5th-magnitude star under the same 10-second exposure but with an increased EM gain of 500. This enhanced multiplication gain improves the detection capability for faint targets. Additionally, a cosmic ray event can be observed in the image. This charge caused by a cosmic ray is also amplified by the EM multiplication process and exceeds the full-well capacity of the multiplication register, causing horizontal trailing in the image. During data reduction, the trails can be partially removed by fitting their profile. However, the inherent photon noise within the trail itself cannot be eliminated. If a trail falls within the dark holes, it may degrade the signal-to-noise ratio (SNR) of the target. To reduce the impact of cosmic rays, careful planning of observations is needed. While long frame exposure times and high EM gain reduce the impact of readout noise, they simultaneously increase the number of cosmic ray events in each frame and raise the probability of cosmic rays exceeding the full-well capacity of the EM register. Thus each observation run demands optimization of exposure time and EM gain settings, and the CPISM program has potential to be used to verify and evaluate the optimization.

4 SUMMARY

CPI-C is a specialized high-contrast imaging instrument for exoplanet studies on the CSST. To support the development of its data reduction system and the evaluation of its scientific performance, we have developed an image simulation program CPISM. In Zhu et al. (2025), we introduced the overall simulation program and the observation target simulation module, and presented a preliminary analysis of the CPI-C's scientific observation capabilities. This paper is the second in the series, in which we introduce the simulation of the coronagraph instrument, focusing on two core modules: the high-contrast imaging module and the EMCCD camera module.

For the high-contrast imaging module, based on the HCIPy package, we modeled the core high-contrast imaging components such as the pupil apodization filter, the wavefront corrector, and the focal plane mask. We also considered the effects of a wide spectral band, and generated a high-contrast imaging dark zone that is similar to the measured morphology and meets the technical requirements. During the optimization of the high-contrast imaging dark zone, we explored the use of electric field conjugation methods for dark zone contrast optimization, which is also the first application of this method in pupil transmission modulation high-contrast systems similar to CPI-C.

For the EMCCD module, we modeled various effects during the image collection process, transfer process, EM multiplication process, and readout process, achieving simulation images that are very close to the actual instrument images. These simulation images contain rich details, providing input for the development of the CPI-C data reduction pipeline. In the simulation of the EMCCD, to accelerate the modeling of the EM multiplication process, we proposed a more accurate formula for the EMCCD multiplication noise distribution. This formula can also be applied to fields such as EM gain fitting.

Acknowledgements This work is supported by the project of the CSST scientific data processing and analysis system of the China Manned Space Project. We thank the anonymous referee for valuable comments that have significantly improved the manuscript. This work is supported

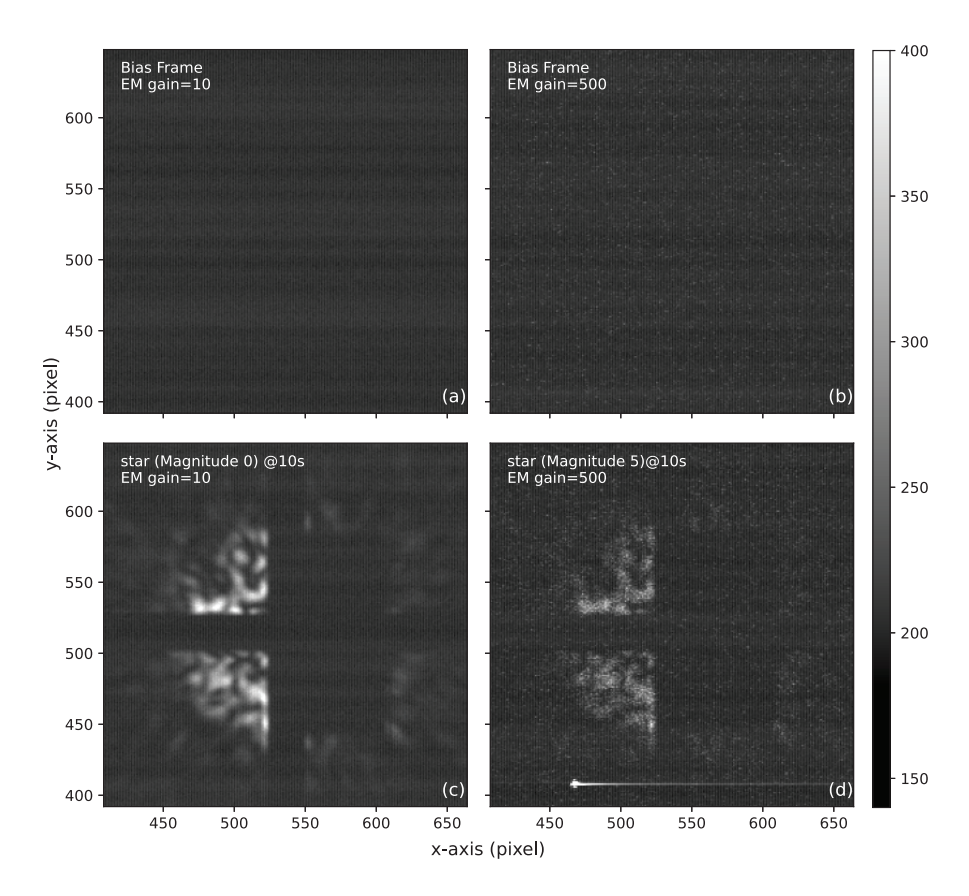


Fig. 9: Examples of simulated images of CPI-C's visible band camera. (a) Bias image with a multiplication gain of 10. (b) Bias image with EM gain 500. (c) 10-second exposure image of a 0th-magnitude star. (d) 10-second exposure image of a 5th-magnitude star with EM gain 500.

by the National Natural Science Foundation of China (NSFC) under grant nos U2031210 and 11827804, as well as the science research grants from the China Manned Space Project (CMS-CSST-2021-A11, CMS-CSST-2021-B04, CMS-CSST-2025-A17, CMS-CSST-2025-A18, CMS-CSST-2025-A19) and the Pre-research project on Civil Aerospace Technologies funded by China National Space Administration (No. D010301).

Appendix A: ELECTRIC FIELD CONJUGATION OPTIMIZATION METHOD

The core objective of the Electric Field Conjugation (EFC) optimization is to iteratively minimize residual starlight within a designated region of the focal plane, forming a high-contrast "dark hole" (DH). The EFC process in the CPISM simulation follows (Matthews 2017) and the document of the HCIPy package. 6 .

Consistent with the CPI-C design parameters, the target dark hole for optimization was defined as a single-sided region extending from an inner working angle (IWA) of 3 λ/D to an outer working angle (OWA) of 16 λ/D . The simulation models the main optical path of CPI-C, including modeled system aberrations, the transmission apodizing filter, the wavefront corrector, up to the final focal plane. Crucially, instead of simulating detector readout and noise,

 $^{^{6}\} https://docs.hcipy.org/0.6.0/tutorials/ElectricFieldConjugation/ElectricFieldConjugation.html$

the optimization process directly accesses the complex electric field data generated at the focal plane.

As the first step of EFC optimization, we calculate the Jacobian matrix G of the system, which links the command voltages applied to the wavefront corrector's actuators to the resulting complex electric field within the DH. We numerically simulate the "poke" method, in which we sequentially apply small, calibrated perturbations $(\pm \delta u)$ to each individual actuator of the DM model and record the corresponding change in the complex electric field vector $E_{\rm DH}$ within the designated DH region. The i-th column of the Jacobian has the form of:

$$\mathbf{g}_{i} = \frac{\partial E_{\mathrm{DH}}}{\partial u_{i}} \approx \frac{E_{\mathrm{DH}}(u_{i} + \delta u) - E_{\mathrm{DH}}(u_{i} - \delta u)}{2\delta u}$$
(A.1)

where $E_{\rm DH}(u_i \pm \delta u)$ denotes the complex electric field vector in the DH when only the *i*-th actuator's command is perturbed by $\pm \delta u$ from a base state.

As the Jacobian matrix G can be ill-conditioned or non-square, directly inverting it to find the correction commands is often numerically unstable. To address this, Tikhonov regularization is employed to compute a stable, regularized pseudo-inverse G_{λ}^{\dagger} of the Jacobian. After finding the Jacobian matrix, we optimize the dark hole by iteration. For each iteration

k:

- 1. The current complex electric field E_k within the DH is obtained. As mentioned, in this simulation, this step is simplified by directly accessing the field E_k from the optical propagation
- 2. Based on the measured field E_k and the regularized pseudo-inverse G_{λ}^{\dagger} , a correction voltage command Δu_k for the wavefront corrector is calculated as:

$$\Delta u_k = -\gamma G_\lambda^{\dagger} E_k \tag{A.2}$$

where γ is the loop gain $(0 < \gamma \le 1)$ to moderate the correction step size.

3. The total voltage command vector applied to the wavefront corrector is updated for the next iteration: $u_{k+1} = u_k + \Delta u_k$.

This iterative process continues until a desired contrast level in the DH is achieved or a maximum number of iterations is reached.

In summary, to generate a dark hole in simulation with characteristics closely resembling the design goals of CPI-C, we utilized the EFC method for focal plane wavefront control. The resulting optimized dark hole spans the 3-16 λ/D region and achieves a contrast level of approximately 10^{-8} , consistent with the instrument's target performance. Since EFC is a modelbased optimization technique, EFC takes advantage of the simulation where the system model is explicitly defined. Furthermore, the simulation environment allows direct access to the complex electric field, greatly simplifying the sensing step compared to real optimization, which requires sophisticated estimation techniques. Implementing EFC on the actual instrument would be a challenge related to model accuracy, calibration, and real-time electric field estimation from detector images. In future work, we will explore the potential use of EFC in the transmission apodization coronagraph system, such as the next generation of CPI-C.

Appendix B: PARAMETERS OF CPI-C INSTRUMENT

In Table B.1, we list key parameters for the CPI-C instrument currently configured in our simulation program. It should be noted that most parameters are currently set according to the instrument's design specifications or requirement values. In future software versions, we will update these parameters based on ground-based or in-orbit measured values.

Table B.1: Parameters of CPI-C instrument used in CPISM

Parameter Name	Parameter Value or Range
Dark zone contrast	1×10^{-8}
Inner working angle (IWA)	$3 \lambda/D$; $0.205''@662 nm$
Outer working angle (OWA)	$16 \lambda/D$; $1.09''@662 nm$
Width of the cross-shape focal mask	0.4''
Focal plane scale	$1.615 \times 10^{-2} ''/\text{pix}$
Camera effective pixels	1024×1024
Field of view (FOV)	$16.54'' \times 16.54''$
Read noise $(1 \times EM gain)$	$160\mathrm{e^-/pix}$
Clock induced charge (CIC)	$0.2\mathrm{e^-/pix}$
Dark current	$1.0 \times 10^{-3} e^{-/pix/s}$
Conversion gain $(1 \times EM gain)$	$59\mathrm{e^-/ADU}$
Full-well capacity of image region	$80000\mathrm{e^-}$
Charge handling capacity of multiplication register	$500000{ m e}^-$
Readout time	$0.365\mathrm{s}$

Table C.1: List of Acronyms and Technical Terms

Acronym	Full Term
CPI-C	Cool Planets Imaging Coronagraph
CSST	China Space Station Telescope
CPISM	CPI-C Image Simulator
CGI	Coronagraph Instrument
JWST	James Webb Space Telescope
PSF	Point Spread Function
IWA	Inner Working Angle
OWA	Outer Working Angle
EFC	Electric Field Conjugation
SPGD	Stochastic Parallel Gradient Descent
FOV	Field of View
SED	Spectral Energy Distribution
PTC	Photon Transfer Curve
ADI	Angular Differential Imaging
LOCI	Locally Optimized Combination of Images
OIRS	Optimized Image Rotation and Subtraction
CCD	Charge-Coupled Device
EMCCD	Electron Multiplying Charge-Coupled Device
CIC	Clock Induced Charge
CTI	Charge Transfer Inefficiency
ADC	Analog-to-Digital Conversion
MEMS	Micro-electromechanical Systems
$_{\mathrm{DM}}$	Deformable Mirror

Appendix C: LIST OF ACRONYMS

In Table C.1, we list all of the acronyms in the paper for reference.

References

Bao, C., Ji, J., Zhao, G., et al. 2025, Direct Imaging for the Debris Disk around \$\varepsilon\$\$\$ Eridani with the Cool-Planet Imaging Coronagraph, arXiv:2509.16761, accepted by RAA 3

Basden, A. G., Haniff, C. A., & Mackay, C. D. 2003, Monthly Notices of the Royal Astronomical Society, 345, 985–10

CSST Collaboration, Gong, Y., Miao, H., et al. 2025, Introduction to the Chinese Space Station Survey Telescope (CSST), arXiv:2507.04618 2

- Daigle, O., Veilleux, J., Grandmont, F., et al. 2022, in Space Telescopes and Instrumentation 2022: Optical, Infrared, and Millimeter Wave, ed. L. E. Coyle, M. D. Perrin, & S. Matsuura (Montréal, Canada: SPIE), 148–8
- Dong, B., Ren, D.-Q., & Zhang, X. 2011, Research in Astronomy and Astrophysics, 11, 997
 Dou, J.-P., Zhang, X., Zhao, G., et al. 2025, Research in Astronomy and Astrophysics, submitted
- Dou, J., & Ren, D. 2016, The Astrophysical Journal, 832, 84 2, 4, 5, 7
- Dou, J., Ren, D., Zhao, G., et al. 2015, The Astrophysical Journal, 802, 12 6
- Douglas, E. S., Ashcraft, J. N., Belikov, R., et al. 2020, Space Telescopes and Instrumentation 2020: Optical, Infrared, and Millimeter Wave, 148 2
- Girard, J. H., Blair, W., Brooks, B., et al. 2018, 10698, 106983V 2
- Gordon, K. D., Bohlin, R., Sloan, G. C., et al. 2022, The Astronomical Journal, 163, 267 2
- Heyer, I., Biretta, J., & et al. 2004, WFPC2 Instrument Handbook, Version 9.0, Tech. rep., Space Telescope Science Institute, Baltimore 2
- Lafreniere, D., Marois, C., Doyon, R., Nadeau, D., & Artigau, E. 2007, The Astrophysical Journal, 660, 770 6
- Marois, C., Lafreniere, D., Doyon, R., Macintosh, B., & Nadeau, D. 2006, The Astrophysical Journal, 641, 556 6
- Matthews, C. T. 2017, Journal of Astronomical Telescopes, Instruments, and Systems, 3, 1 5, 15
- Miles, B. E., Biller, B. A., Patapis, P., et al. 2023, The Astrophysical Journal Letters, 946, L6
- Miles, N. D., Deustua, S. E., Tancredi, G., et al. 2021, The Astrophysical Journal, 918, 86 2 Por, E. H., Haffert, S. Y., Radhakrishnan, V. M., et al. 2018, in Adaptive Optics Systems VI,
- ed. D. Schmidt, L. Schreiber, & L. M. Close (Austin, United States: SPIE), 152 3
- Pueyo, L., Kay, J., Kasdin, N. J., et al. 2009, Applied Optics, 48, 6296 5
- Ren, D., Dou, J., & Zhu, Y. 2010, Publications of the Astronomical Society of the Pacific, 122, 590 2
- Ren, D., & Zhu, Y. 2007, Publications of the Astronomical Society of the Pacific, 119, 1063–2,
- Robbins, M. 2009, Determining the Multiplication of EMCCD Sensor 12
- Robbins, M., & Hadwen, B. 2003, IEEE Transactions on Electron Devices, 50, 1227 11
- Trauger, J., Moody, D., Krist, J., & Gordon, B. 2016, Journal of Astronomical Telescopes, Instruments, and Systems, 2, 011013 6
- Tubbs, R. N. 2003, Lucky Exposures: Diffraction Limited Astronomical Imaging through the Atmosphere, arXiv:astro-ph/0311481 10
- Tulloch, S. 2010, Astronomical Spectroscopy with Electron Multiplying Ccds, PhD thesis, Department of Physics & Astronomy, The University of Sheffield, Sheffield, UK 10
- Tulloch, S. M., & Dhillon, V. S. 2011, Monthly Notices of the Royal Astronomical Society, 411, 211 8
- Turnbull, M. C., Zimmerman, N., Girard, J. H., et al. 2021, Journal of Astronomical Telescopes, Instruments, and Systems, 7 2
- Ygouf, M., Zimmerman, N., Bailey, V., et al. 2021, Roman Coronagraph Instrument Post Processing Report - OS9 HLC Distribution, Tech. Rep. April 3, Jet Propulsion Laboratory, California Institute of Technology; Goddard Flight Space Center; Space Telescope Science Institute, Pasadena, CA 2
- Zhu, Y.-M., Zhao, G., Chen, Y.-L., & Dou, J.-P. 2025, Research in Astronomy and Astrophysics, accepted 3, 14